Eur. Phys. J. A (2018) **54**: 66
DOI 10.1140/epja/i2018-12500-0

THE EUROPEAN PHYSICAL JOURNAL A

Regular Article – Experimental Physics

Fission fragment yields from heavy-ion–induced reactions measured with a fragment separator

O.B. Tarasov[1,a,b], O. Delaune[2,c], F. Farget[2], D.J. Morrissey[1,3], A.M. Amthor[4], B. Bastin[2], D. Bazin[1], B. Blank[5], L. Cacéres[2], A. Chbihi[2], B. Fernández-Dominguez[6], S. Grévy[5], O. Kamalou[2], S.M. Lukyanov[7], W. Mittig[1,8], J. Pereira[1], L. Perrot[9], M.-G. Saint-Laurent[2], H. Savajols[2], B.M. Sherrill[1,8], C. Stodel[2], J.C. Thomas[2], and A.C. Villari[10]

[1] National Superconducting Cyclotron Laboratory, MSU, East Lansing, MI 48824, USA
[2] Grand Accelerateur National d'Ions Lourds, CEA/DRF-CNRS/IN2P3, F-14076 Caen, France
[3] Department of Chemistry, Michigan State University, East Lansing, MI 48824, USA
[4] Department of Physics, Bucknell University, Lewisburg, PA 17837, USA
[5] CENBG, UMR 5797 CNRS/IN2P3, Université de Bordeaux, F-33175 Gradignan, France
[6] Universidade de Santiago de Compostela, E-15782 Santiago de Compostela, Spain
[7] FLNR, JINR, Dubna, Moscow region, 141980, Russia
[8] Department of Physics and Astronomy, MSU, East Lansing, MI 48824, USA
[9] IPN Orsay, CNRS/IN2P3, F-91406 Orsay, France
[10] Facility for Rare Isotope Beams, MSU, East Lansing, MI 48824, USA

Received: 17 November 2017 / Revised: 26 February 2018
Published online: 26 April 2018 –
Communicated by P. Woods

Abstract. The systematic study of fission fragment yields under different initial conditions has provided valuable experimental data for benchmarking models of fission product yields. Nuclear reactions using inverse kinematics coupled to the use of a high-resolution spectrometer with good fragment identification are shown here to be a powerful tool to measure the inclusive isotopic yields of fission fragments. In-flight fusion-fission was used in this work to produce secondary beams of neutron-rich isotopes in the collisions of a ^{238}U beam at 24 MeV/u with ^{9}Be and ^{12}C targets at GANIL using the LISE3 fragment separator. Unique identification of the A, Z, and atomic charge state, q, of fission products was attained with the ΔE-TKE-$B\rho$-ToF measurement technique. Mass, and atomic number distributions are reported for the two reactions. The results show the importance of different reaction mechanisms in the two cases. The optimal target material for higher yields of neutron-rich high-Z isotopes produced in fusion-fission reactions as a function of projectile energy is discussed.

1 Introduction

1.1 In-flight separated fusion-fission as a new mechanism to produce rare isotope beams

Fission of heavy nuclei is a useful tool to produce neutron-rich isotopes of interest for basic research. The production of fission fragments by light-ion or neutron bombardment of heavy targets in so-called normal kinematics suffers from difficulties with fragment extraction from the target and identification of the slow moving fragments. On the other hand, in-flight fission using inverse kinematics can be a useful production method in which the fast moving fragments are relatively easy to separate and identify. Pioneering in-flight fission experiments at high energy at GSI explored neutron-rich isotopes with $Z = 28$–60 [1]. Since that time, in-flight fission has been widely used to produce rare neutron-rich nuclei and experiments have used different mechanisms to induce the fission process at relativistic energies [2]. At large impact parameters with high-Z targets, the long-range Coulomb force prevails (Coulomb fission). For slightly smaller impact parameters, peripheral nuclear collisions take place and the fissile projectile is left abraded and excited. During the de-excitation process, it can undergo fission with a high probability (abrasion-fission) [2,3]. This paper explores the use of fusion-fission in inverse kinematics to produce beams of rare isotopes. Recent experiments using the VAMOS spectrometer to measure fission fragment yields from the reaction of ^{238}U

[a] e-mail: tarasov@nscl.msu.edu
[b] *On leave from*: FLNR/JINR, Dubna, Moscow Region, 141980, Russia.
[c] *Present address*: CEA DAM DIF, F-91297 Arpajon, France.

with ^{12}C at near Coulomb barrier energies have demonstrated the advantage of this approach [4], and the ability to measure general properties of transfer- and fusion-induced fission fragment distributions [5–7].

Experiments in inverse kinematics using fragment separators or magnetic spectrographs have the problem that it is difficult to collect all fragments in a limited solid angle and the observed yields strongly depend on the magnetic system used. In the present work a new simulation based on a recent model [8] was developed to carry out fast calculations of the fusion-fission (FF) fragment yields including the cross sections, reaction kinematics, and spectrometer acceptances in order to facilitate studies of fusion-fission. The model was implemented in the LISE^{++} package [3] and incorporated existing analytical descriptions of fusion-evaporation and fission fragment production mechanisms. The advantages of in-flight fusion-fission in inverse kinematics to explore the neutron-rich $55 < Z < 75$ region are shown in comparison to the abrasion-fission and Coulomb fission processes. An important feature of inverse kinematics is that the excitation energy delivered to the heavy nucleus can be relatively low even though the laboratory kinetic energy is high. The predictions are compared to the results of an experiment performed with the LISE3 spectrometer [9] to separate and identify such fusion-fission products, and the comparisons generally agree with the LISE^{++} simulation with the recent fusion-fission model.

1.2 Reaction mechanism and fusion-fission isotope yields

The cross section for the complete fusion of two colliding nuclei forming a compact excited compound nucleus (CN) at an excitation, E^*, and angular momentum, J, can be written as

$$\sigma_{CN}\left(E^*, J\right) = \sigma_{capture}\left(E^*, J\right) P_{CN}\left(E^*, J\right), \qquad (1)$$

where $\sigma_{capture}$ is the cross section for the formation of the dinuclear system (capture), and P_{CN} is the probability to form a CN with a compact shape. The complementary process to the CN formation in the heaviest nuclei is quasifission (QF) with probability $1-P_{CN}$. Quasifission is a transitional mechanism between deep-inelastic collisions and complete fusion in which the composite system separates in two large fragments without forming a CN [10]. The excited CN formed in a fusion reaction can undergo fission, or through particle emission produce evaporation residues (ERs)

$$\sigma_{CN}\left(E^*, J\right) = \sigma_{FF}\left(E^*, J\right) + \sigma_{ER}\left(E^*, J\right). \qquad (2)$$

Fragment mass distributions from fusion-fission (FF) reactions have been extensively investigated for many years [10,11] as they provide important information on fission dynamics. Along with QF reactions [10,12–14], FF is the most important reaction mechanism present in reactions with the heaviest nuclei. In fact, the formation probability of super heavy elements in fusion reactions is thought to be determined by the fusion-fission process [10, 14,15]. The present work describes a method to obtain additional information on the isotopic fission-fragment yields over the entire atomic-number range of the fission fragments (*i.e.*, from $Z = 30$ to $Z = 64$) using inverse kinematics coupled with a fragment separator. Recent data from the LISE3 separator was used in the present case.

The FF reactions were induced by a ^{238}U beam at an energy of 24 MeV/u impinging on a 15 mg/cm^2 thick ^{9}Be metal or natural carbon target. The main reaction channels and their general characteristics are listed in table 1 as a function of characteristic angular momenta associated with each reaction. The table provides a framework for describing the yields observed in FF experiments. Note that the beam energy was approximately 20 MeV/u in the middle of these targets so that the excitation energies of the compound nuclei are moderate due to the large center of mass motion, as seen in table 1. FF clearly dominates over ER at these high excitation energies and fissilities (*e.g.*, $E^* = 140$–200 MeV and 170–250 MeV, CN fissility parameters [16] $x_{CN} = 0.804$ and 0.823 for CN formed with Be and C targets respectively). The extreme entrance channel asymmetry of these reactions $\alpha = (A_2 - A_1)/(A_2 + A_1) = 0.927$ (0.904), and low atomic-number product $Z_pZ_t = 368$ (552) for Be (C) targets generally hinders dissipative effects in the collision stage of the reaction and strongly suppresses the QF mechanism [14,17,18].

2 Experimental measurement

A ^{238}U^{58+} beam was accelerated to 24 MeV/u with an intensity on the order of 10^9 ions/s with the CSS1 and CSS2 cyclotrons at GANIL. The beam was directed onto the LISE3 target at an angle of 3° to prevent the unreacted beam from entering the spectrometer, as indicated schematically in fig. 1.

Considering the high kinetic energy of the excited heavy nuclei produced in the collision, most of the reactions lead to the emission of fission fragments in a cone of approximately 10° around the beam direction. The small proportion that entered the LISE3 spectrometer, due to the finite solid angle, were then identified by the combination of magnetic-rigidity $B\rho$, time-of-flight (ToF), total kinetic energy (TKE), and energy-loss (ΔE) measurements. The identification of heavy ions using this technique was described in detail in the appendix of ref. [19]. Two position-sensitive micro-channel plate detectors [20] were used to measure the position of the particles at the intermediate dispersive plane, X_{31}, and at the final focal plane, X_{62}, as indicated in fig. 1, to deduce the magnetic rigidity of the particles.

The spectrometer sections before and after the intermediate focal plane (slits 31) were set to the same magnetic rigidity. The position calibrations of the micro-channel detectors (Gallote 31, Gallote 62) were performed using slits placed in front of each detector. The spectrometer's ion-optical parameters (dispersions and magnifications) were calibrated by measurements of the positions

Table 1. Angular momenta that separate reaction channels and characteristic parameters for reactions of ^{238}U (20 MeV/u) with ^{9}Be and ^{12}C. The values of the classical angular momenta [21,22] were calculated by the LISE^{++} code for the fusion reaction mechanism [23]. The Sierk model [24] was used to estimate the dependence of the fission barrier, B_{fis}, on angular momentum.

	L ($B_{fis} = 0$)	L *critical*	L *direct*	L *max* ("*grazing*")
Reaction characteristic	fission barrier of CN vanishes	the maximum angular momentum for fusion, the first L without a minimum in the total internuclear potential energy [21]	at the distance when the colliding nuclei touch (interaction radius) [21,22]	at the distance of closest approach; corresponds to grazing angle [22]
Be-target	67 $\hbar$	75 $\hbar$	78 $\hbar$	89.2 $\hbar$
C-target	63 $\hbar$	87 $\hbar$	99 $\hbar$	117.1 $\hbar$
From adjacent lower L up to this L	complete fusion-fission	fast-fission with high excitation (HE), heavy products undergo sequential fission [25]	deep-inelastic collisions with HE, sequential fission	some direct reactions (QE) lead to low excitation fission
Z of fissioning nucleus	compound nucleus: Be: $Z = 96$; C: $Z = 98$	below projectile $85 < Z < 92$		near projectile $Z = 92$
Velocity of fissioning nucleus	compound velocity	between compound and projectile velocities		close to projectile velocity
Excitation energy of fissioning nucleus	at $L = 0$ C: 204.3 MeV Be: 166.6 MeV	very broad energy range (30 MeV up to CN excitation energy)		low energies: 6–30 MeV
Z-distribution of fission fragments	one broad peak at Be: $\langle Z \rangle = 48$ C: $\langle Z \rangle = 49$	broad distribution with peak at $Z \sim 42$–45		two narrow peaks at $Z \sim 38$–41 and 52–54
Reaction channel designation	FF (fusion-fission)	FA (fast fission)		IF (asymmetric fission)

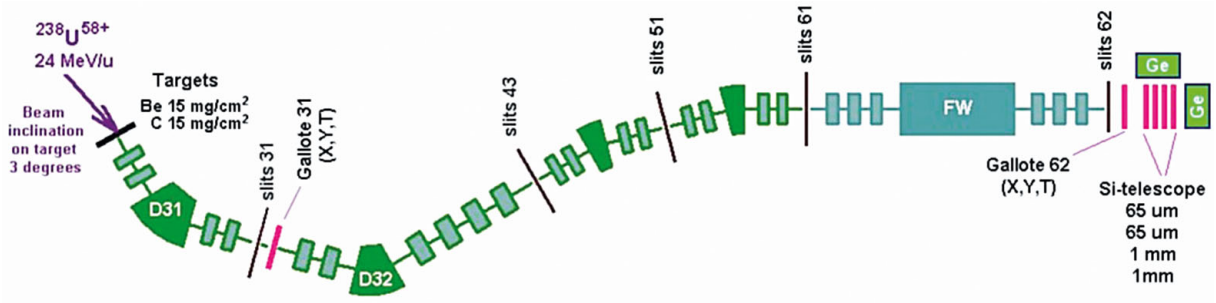

Fig. 1. Schematic layout of the LISE3 spectrometer with the detection equipment for the identification of fission fragments.

of different charge states of the primary beam. A stack of four silicon detectors was installed after the second microchannel plate detector (Gallote 62) to measure the energy loss rate and the total kinetic energy of the ions. Four Time-of-Flight (ToF) measurements of each fragment were performed during the experiment using:

- Gallote 31 and Gallote 62;
- Gallote 31 and 1st silicon detector at the final focal plane (FFP);
- 1st silicon detector at FFP and the arrival time relative to the phase of the cyclotron rf-signal;
- 2nd silicon detector at FFP and the arrival time relative to the phase of the cyclotron rf-signal.

The flight paths were assumed to be independent of the measured positions on the detectors and taken to be 35.003, 35.243, 42.828, and 42.838 m [9], respectively, for the combinations listed above. The first and second measurements both gave excellent timing resolution providing good mass resolution, but the highest efficiency for low-Z fragments was obtained with the second method (Galotte31 *vs.* 1st silicon detector at FFP) and was used in the analysis.

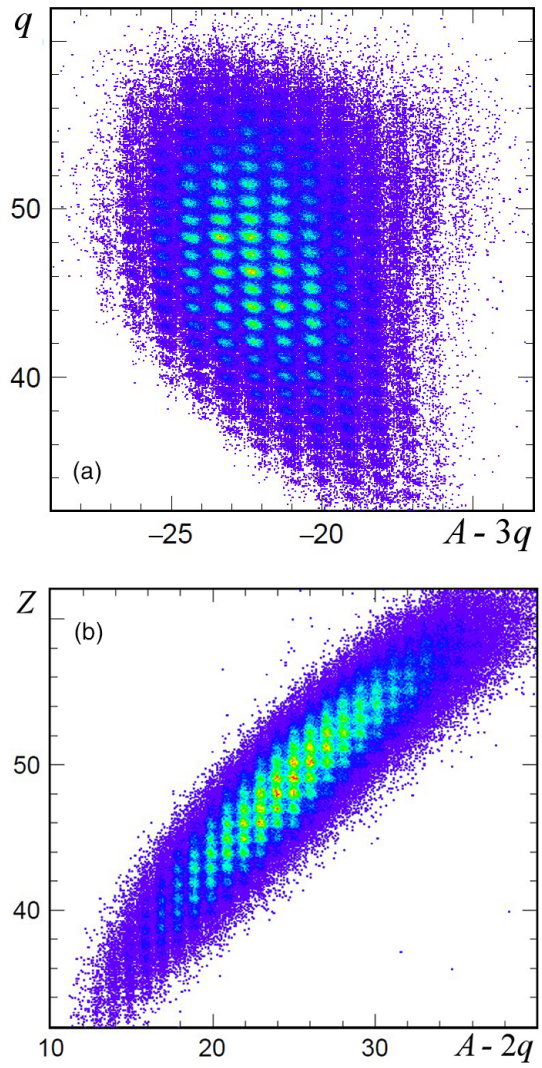

Fig. 2. (a) Ionic charge, q, *versus* $A - 3q$ particle identification (PID) diagram measured for the nominal magnetic rigidity $B\rho = 1.9\,\mathrm{Tm}$ with the Be target. (b) Proton number, Z, *versus* $A - 2q$ PID diagram for the same spectrometer settings.

The particle identification (PID) diagram with the ionic charge q *versus* the quantity $A - 3q$ deduced from measured values, where A is the mass number, measured with the Be target for the nominal magnetic rigidity $B\rho = 1.9\,\mathrm{Tm}$ is displayed in fig. 2(a). This figure demonstrates mass and ionic charge resolution of $\mathrm{FWHM}(A)/A_{(A=100,140)} = 0.55\%$, 0.49%, and $\mathrm{FWHM}(q)/q_{(q=52)} = 1.1\%$, which provided adequate identification of the products. The atomic number Z of each fragment was identified with the energy-loss measurement in the first silicon detector of the silicon stack ($69\,\mu\mathrm{m}$ thick). The atomic number Z *versus* the quantity $A - 2q$ particle identification (PID), shown in fig. 2(b), demonstrates the atomic number resolution $\mathrm{FWHM}(Z)/Z_{(Z=44,54)} = 1.68\%$, 1.61% due to the use of a thin detector.

The isotopic identification was confirmed by the observation of the gamma-ray decay of short-lived isomeric states in several fission fragments observed in two germanium detectors placed near the silicon stack. Figure 3 illustrates the confirmation of the PID by observation of gamma rays from ^{128m}Te decay, following implantation of identified ^{128}Te ions in the stack.

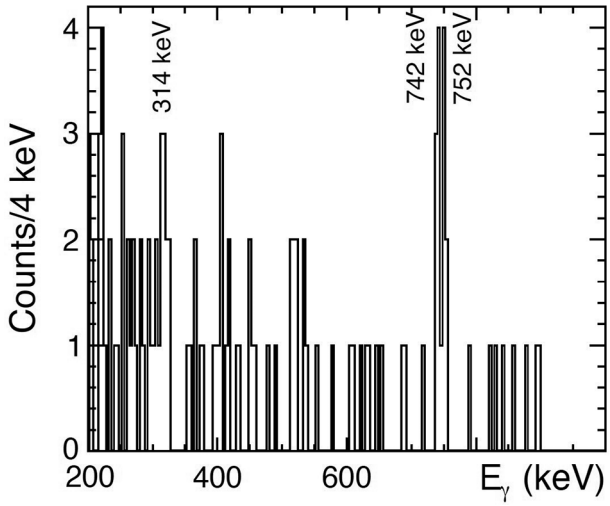

Fig. 3. Gamma-ray spectrum observed in coincidence with ^{128}Te. The characteristic gamma lines of 314, 742 and 752 keV from the decay of the known $T_{1/2} = 370\,\mathrm{ns}$ isomeric state.

2.1 Beam charge-state distribution

Prediction of the charge state distribution of the various fragments was important and a series of auxiliary measurements was carried out as part of this work. The momentum dispersion of 1.8 cm/% at the Gallote 31 position allowed the measurement of several charge-states of the uranium beam at a single magnetic-field setting and allowed a determination of the beam charge-state distribution after passing through various materials. The exact rigidity differences between the observed charge states also provided an absolute calibration of the spectrometer. The magnetic rigidity of the spectrometer was scanned in order to cover the charge-state distribution of the beam. The resulting distributions are displayed in fig. 4 and are compared to three different parameterizations typically used to describe heavy-element charge state distributions at this energy [26–28]. Note that the beam enters the foils with $q = 58$ while the equilibrium charge state is near $q = 80$. Panels (a) and (c) in fig. 4 show the beam charge-state distributions after passing through a thin carbon ($40\,\mu\mathrm{g/cm^2}$) and an $15\,\mu\mathrm{g/cm^2}$ Mylar foil with $20\,\mu\mathrm{g/cm^2}$ Al, respectively. It is clear that these thin carbon foils only slightly increase the charge state of the incoming beam, while the Mylar foil produced a distribution that was almost halfway to the equilibrium value. Note that the three parameterizations assume that the material is thick enough to attain the equilibrium charge state and thus show a large discrepancy with the data. Panels (b) and (d) show the beam charge state distributions after passing through a $3\,\mathrm{mg/cm^2}$ aluminum and

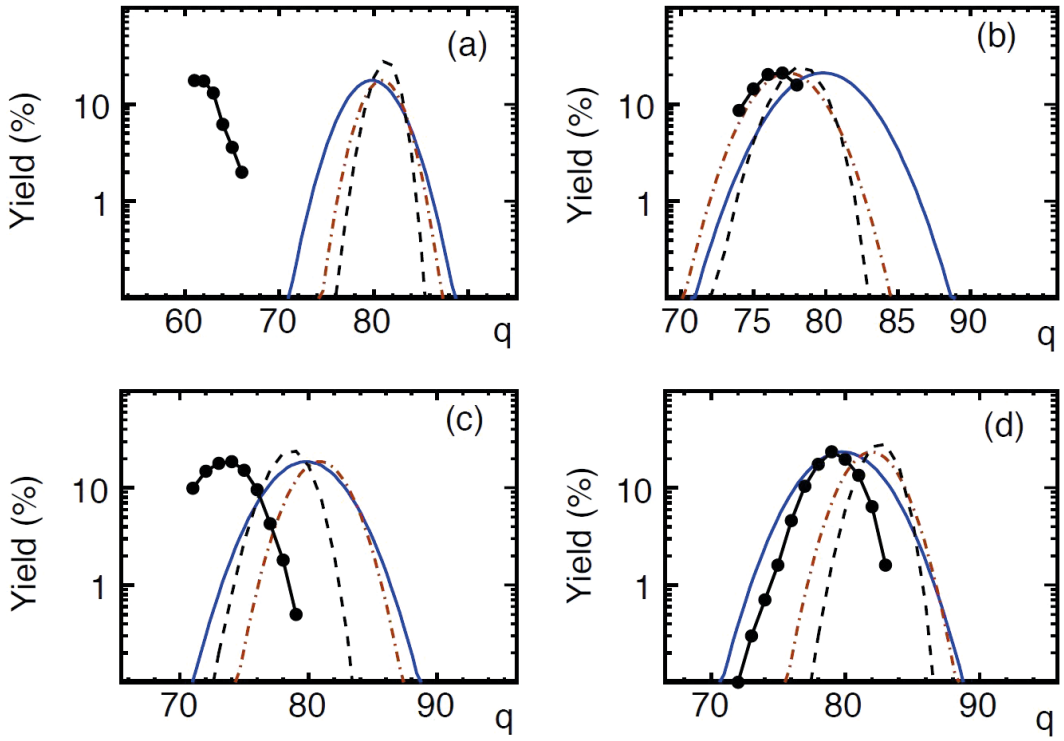

Fig. 4. Primary beam charge state distributions measured after passing through various materials. (a) 40 μg/cm^2 C; (b) 3 mg/cm^2 Al, (c) 15 μg/cm^2 Mylar foil with 20 μg/cm^2 Al; (d) 1.4 mg/cm^2 Be. The data are compared to parameterizations of the charge-state distributions in the literature: Schiwietz [27] (solid blue line), Leon [26] (dot-dashed red line), and Winger [28] (black dashed line). The uncertainties in the relative yields are generally smaller than the points in this figure due to the very large number of events observed for each charge state of the beam.

a 1.4 mg/cm^2 beryllium foil, respectively, that are thick enough to reach the equilibrium charge-state. The widths of Gaussian functions fitted to these distributions are $\sigma_a = 2.24$, $\sigma_b = 1.79$, $\sigma_c = 2.24$, and $\sigma_d = 1.78$. In cases (b) and (d) the narrow distributions indicate that equilibrium was reached, and the calculations show better agreement with the data. The Leon parameterization [26] gives excellent agreement with data from the thick Al foil, whereas the predicted mean charge state is too high in the case of the Be foil. In both cases, the Schiwietz model [27] gives a fair prediction of the average charge state, while the width of the predicted distribution is too large. The Schiwietz parameterization gives the best description of the distribution from the thick foil (d) and with the fragment charge state distribution measurement (described in the next chapter) was used in the analysis of the rest of the data.

3 Reconstruction of the fission fragment yields

The angular acceptance of the separator only allowed a fraction of the full angular distributions of the fission fragments to be collected at one time. A related limit existed for fragment momentum distributions due to the limited separator momentum acceptance. The angle-aperture of the spectrometer was $\pm 1°$, the beam was incident off-axis, and the momentum acceptance was set to $\pm 0.8\%$ by Slits 31 in the dispersive focal plane in front of Gallote 31 (see fig. 1). Fragment production was measured at four different rigidity values and, in order to span as much as possible of the fragment momentum distribution, the four central momenta were separated by approximately 5% each.

Figure 5 shows a comparison between the experimental charge-state distribution measured for a ^{96}Zr and a ^{120}Sn fragment from the ensemble of spectrometer settings along with the results of the simulation. The good agreement between the simulated and measured charge-state distributions gives confidence that the simulation of the kinematics and the charge state distributions are reasonable and should result in an overall error of less than 20% in the final cross sections.

The yields measured at the four different spectrometer settings were normalized to the average incident beam intensity using measurements at the start and end of each run with a Faraday cup inserted at the target position.

Fragment transmission through the separator was calculated with the LISE^{++} code. Abrasion-Fission and Complete Fusion-Fission reactions were used to predict the fission cross sections at each magnetic rigidity setting. Due to the fact that the step size in magnetic rigidity between the measurements was the same, weighting the measured data by the transmission values is equivalent to integration of the data over the full rigidity range. Abrasion-Fission reaction kinematics [29] was chosen to simulate the

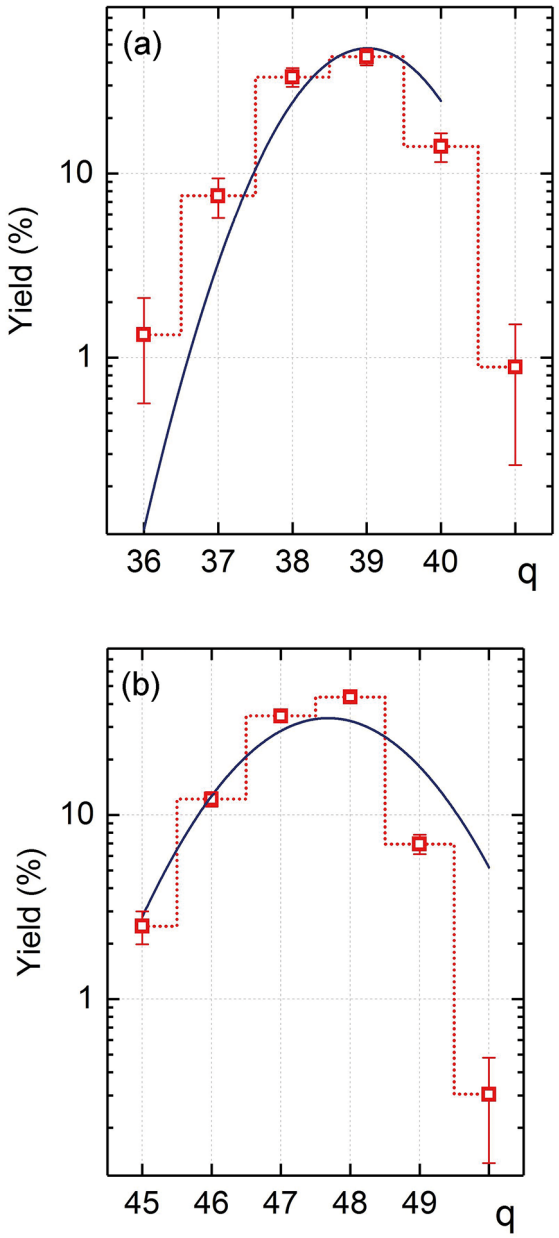

Fig. 5. Red dotted lines: charge state distributions of ^{96}Zr and ^{120}Sn from a 15 mg/cm^2 Be-target in panels (a) and (b), respectively, measured at a magnetic rigidity of $B\rho = 1.9$ Tm. Dark blue solid lines are the results of the simulation described in the text.

transmission of fast-fission (FA) products due to the similarity of the characteristics of the products (see table 1) as both sets of fissile nuclei are slightly lighter than the projectile and have very broad excitation energies. It should be noted that the LISE^{++} fast analytical mode was used and the reaction was assumed to take place in the middle of the target. Therefore, in order to avoid too much averaging in transmission calculations with the rather thick target (15 mg/cm^2), the target was divided into 5 sections in the calculations. This method of combining transmissions for different reaction channels in different slices of the target to obtain cross sections should be valid when there are very similar contributions from both channels (here FF and FA).

4 Results and discussion

4.1 Fission cross sections

The fission cross sections were summed over all isotopes and found to be (3.6 ± 1.0) and (2.4 ± 0.7) barns for the Be and C target, respectively. The large errors arise primarily from the method of beam current measurement used in this experiment that had a large uncertainty for relatively low primary beam intensities (< 20 enA). For comparison, the total fission cross sections measured in this work at 20 MeV/u energy in the middle of the target are higher than the 2.00 ± 0.42 and 1.53 ± 0.15 barns observed in high energy interactions of ^{238}U (1 GeV/u) with deuterium [30] and hydrogen [31], respectively.

4.2 Elemental and neutron distributions

Observed normalized yield distributions are shown as a function of the atomic and neutron numbers of the fission fragments in fig. 6. The general features of the distributions are listed in table 2. These results are also compared to those obtained for the reactions of ^{238}U (1 GeV/u) with deuterium [30] and hydrogen [31] targets in the figure. The new results show that heavier fission fragments are produced at low energies and that this tendency is especially true in the case of the beryllium target: on average being approximately 9 and 13 mass units heavier compared to those from the hydrogen [31] and deuterium [30] targets, respectively. Also, the shape of the elemental distribution of fission fragments produced with the beryllium target is somewhat trapezoidal with a plateau from $Z = 46$ to 52 as compared to the more Gaussian shapes obtained with the other targets.

The widths of the fission fragment distributions produced by uranium in this work are shown as a function of atomic and neutron number and compared with high energy results with light targets [30,31] in fig. 7. The mean N/Z ratios are shown in fig. 8 and clearly indicate that more neutron-rich isotopes of elements below $Z = 48$ are produced with the beryllium target at low energy. This target has a lower energy in the center-of-mass compared to the other cases that results in a lower excitation energy of the fissioning nuclei and therefore lower excitation energies of the fission fragments. For example, the calculated weighted-average excitation energies of Zinc ($Z = 30$) fragments after fission of the excited compound nuclei ^{247}Cm ($E^* = 167$ MeV) and ^{250}Cf ($E^* = 204$ MeV), and of the nuclei fissioning after abrasion of ^{238}U by a light target are 58, 70, 125 MeV respectively. Similarly for Bromine isotopes ($Z = 35$) the excitation energies are 69, 82 and 106 MeV, respectively. In addition to these high excitation reaction channels (FF, FA, abrasion-fission), the asymmetric low-energy fission component (IF with a high

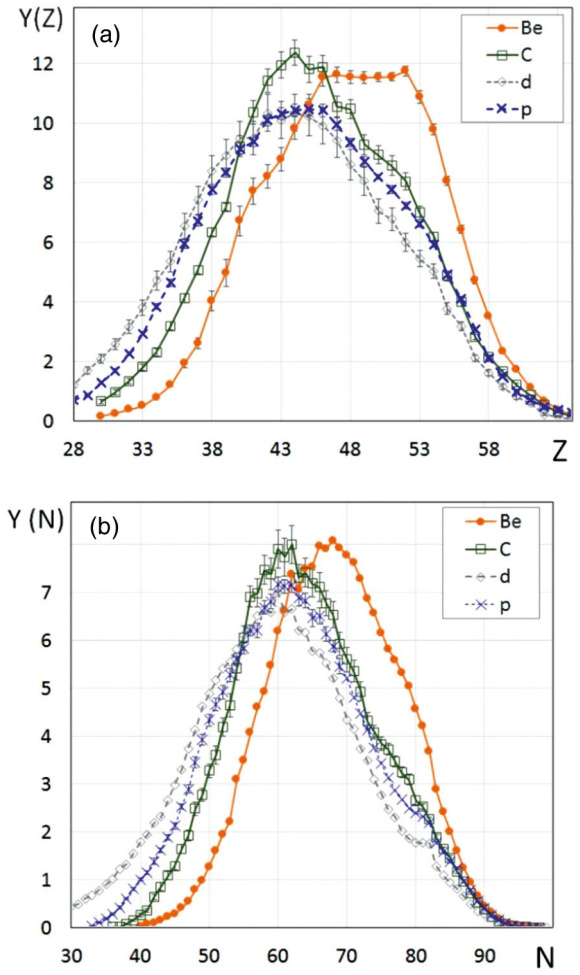

Fig. 6. Atomic (a) and neutron (b) number distributions of fission fragments produced by uranium at 24 MeV/u in this work with Be (solid dot) and C (open square) targets, along with those previously observed at 1 GeV/u with deuterium (open diamonds) [30] and hydrogen (cross) [31].

N/Z contribution [30]) was found to be significantly larger with the beryllium target compared to other cases.

4.2.1 Fission exit channels

As illustrated in table 1, the characteristics of fission product distributions can be attributed to different reaction mechanisms with different fissile nuclei and excitation energies. Hence, it is interesting to see if the LISE^{++} model can describe the observed distributions. The previous descriptions [30,31] of the high energy reactions simply divided the intermediate fissioning nuclei into two groups: a small component with an asymmetric mass distribution from low energy fission and a large, single broad distribution created by a wide range of fission channels. The present low-energy data appear to be more complex. A two-step χ^2-minimization was used to fit the magnitudes and centroids of the predicted fission fragment distributions to the experimental data. In the first step of the analysis, only two high energy excitation fission channels were included for the carbon target: 1) complete fusion forming the compound nucleus with a finite fission barrier (fusion-fission, FF) and fission fragments centered at $Z = 49$, plus 2) capture at higher angular momenta leading to a dinuclear system without a fission barrier (fast-fission, FA) creating fission fragments centered at $Z = 44$ as seen in previous results from the high-energy [30,31]. In the case of the beryllium target with the expectation of a low FA yield, only FF was included in the first step, with fission fragments centered at $Z = 48$. Normal distributions with a width $\sigma_Z = 6$ were used with the constraint that the yield should not exceed the experimental results. This constraint allowed one to then determine the positions of the low-energy asymmetric peaks (IF) after subtraction of FF and FA components in the case of the carbon target. The deduced centroids of Z of the asymmetric fission component at 40.0 and 53.5 (for carbon and beryllium targets, respectively) with $\sigma_Z = 2.0$ were used in the second fitting step along with variation of the FA and IF distribution parameters. The deduced Z-position of the FA component at 46.0 was used for beryllium targets with $\sigma_Z = 2.5$. The second minimization step gave a reduced χ^2 value of 4.0 for the beryllium target data in which all centroid positions were conserved (FA at 45.5, IF at 40.8 and 53.2), whereas for the carbon target some shifts in the centroids were observed (FA at 43.8, IF at 42.0 and 53.4) with χ^2 value of 2.3. It is necessary to note that an asymmetric shape of the IF-left distribution was used for the minimization in the case of beryllium target.

The contributions to the elemental distributions of the fission fragments from the different fission channels from this fitting procedure are shown in fig. 9 and the parameters are given in table 3. For the heavy asymmetric fragments produced at low excitation energy reactions, the maximum positions for both targets were found to be near $Z = 54$, which is in agreement with the previous analysis by Schmidt *et al.* [32]. Note that the sum of low-energy peaks at $Z = 93.5$ and 94.5 for Be and C targets, respectively, slightly exceeds the number of protons in the projectile ($Z = 92$), which indicates a significant contribution from nucleon transfer (or incomplete fusion) from target to projectile in this energy domain.

As can be seen from fig. 9 the fusion-fission mechanism appears to be responsible for high Z isotope production ($Z > 60$) with both targets, as discussed previously [8] and thus shows that in-flight fusion-fission is advantageous for exploring the neutron-rich high Z regions of the nuclear chart using the heavier fissile nucleus.

Asymmetric fission at this energy, as well as at high energies, produced with light targets represents a small fraction of the total fission cross section. The main component in high energy experiments is sequential fission after abrasion of the projectile (abrasion-fission), whereas in the current work fission after the complete fusion (FF) highly dominates over other channels with the Be target, and fusion–fast-fission dominates with the C target.

Table 2. Mean values and widths of the atomic and neutron number distributions (see fig. 6) of fission fragments produced with uranium beams measured in the present work and compared with high energy results.

Target	Energy	$\langle Z \rangle$	σ_Z	$\langle N \rangle$	σ_N	Ref.
Be	24 MeV/u	48.01 ± 0.22	6.03 ± 0.17	68.29 ± 0.18	9.30 ± 0.14	this work
C	24 MeV/u	45.75 ± 0.21	6.40 ± 0.16	64.16 ± 0.17	10.22 ± 0.13	this work
p	1 GeV/u	44.93 ± 0.20	7.00 ± 0.15	62.60 ± 0.16	11.18 ± 0.12	[31]
d	1 GeV/u	43.54 ± 0.20	7.44 ± 0.15	59.83 ± 0.18	12.03 ± 0.12	[30]

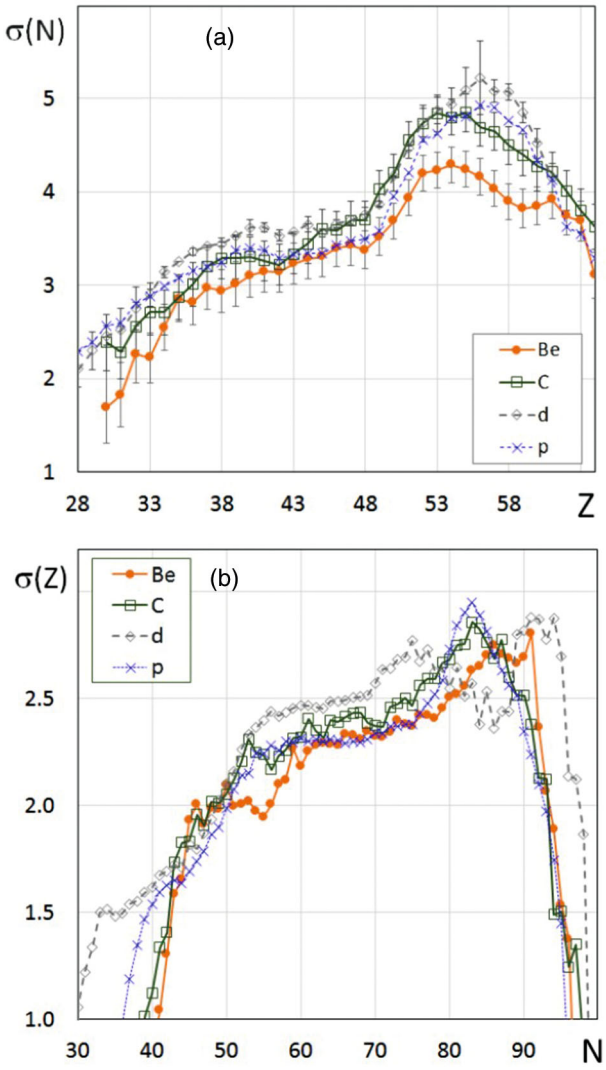

Fig. 7. Distributions of the neutron widths σ_N (a) and atomic number widths σ_Z (b) of fission fragments produced by uranium with energy 24 MeV/u in this work on Be (solid dots) and C (open squares), and with energy 1 GeV/u with deuterium (open diamonds) [30] and hydrogen (crosses) [31].

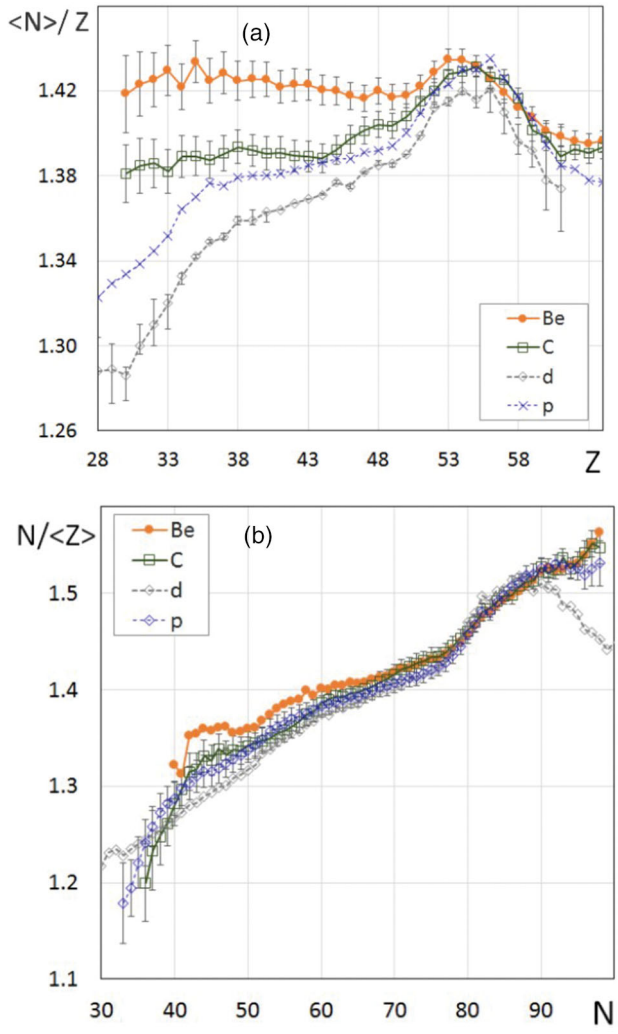

Fig. 8. Mean $\langle N(Z) \rangle / Z$ and $N / \langle Z(N) \rangle$ ratios as a function of Z (a) and N (b) for fission fragments produced by uranium with energy 24 MeV/u in this work on Be (solid dots) and C (open squares), and with energy 1 GeV/u with deuterium (open diamonds) [30] and hydrogen (crosses) [31].

4.3 Comparison with calculations

The LISE^{++} code was used to calculate the overall contribution of each reaction channel in these reactions based on the partial wave description [23] and compared to the experimental results. No quasi-fission is expected in such very asymmetric systems with light targets and hence the fission channel completely dominates in the de-excitation process. The partial cross sections at low angular momentum are predicted to go into the complete fusion-fission channel (FF). The distributions of partial wave cross sections calculated by the LISE^{++} code for the reaction of ^{238}U primary beam at energy 20 MeV/u with beryllium and carbon are shown in fig. 10, and their values are given in table 4.

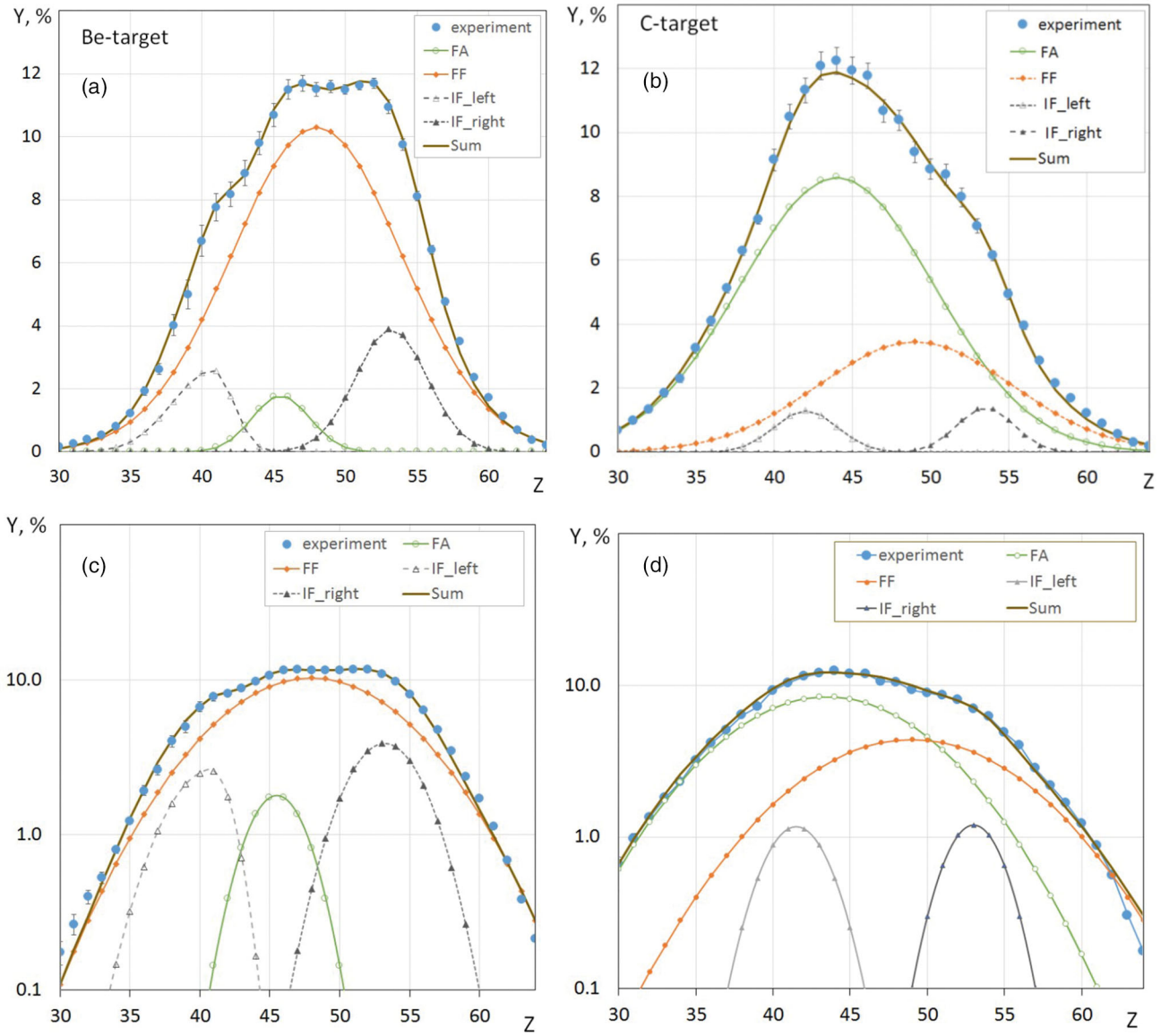

Fig. 9. Elemental fission yields (large blue solid circles) measured in the current work with beryllium ((a), (c)) and carbon ((b), (d)) targets. Top panels represent the elemental yields with a linear scale of vertical axes, while bottom panels display the results on a logarithmic scale. The different fission channel contributions obtained from the fitting procedure are given in table 3. Thick solid lines are sums of fission channels. Fitting details are discussed in the text.

Table 3. Contributions of the independent fission channels determined in this work (see fig. 9), and corresponding cross sections values obtained with use of the total measured fission cross sections.

	Be target		C target	
Fission Channel	contribution	cross section (mb)	contribution	cross section (mb)
Complete fusion-fission (FF)	$76.4 \pm 2.5\%$	2750 ± 770	$26.8 \pm 2.6\%$	650 ± 200
Fast-fission (FA)	$4.5 \pm 4.0\%$	160 ± 150	$66.8 \pm 5.5\%$	1620 ± 480
Incomplete fusion-fission (IF)	$19.1 \pm 4.5\%$	690 ± 250	$6.4 \pm 4.8\%$	155 ± 100
Ratio FF/(FF+FA)	$94.4 \pm 7.2\%$		$28.6 \pm 3.3\%$	

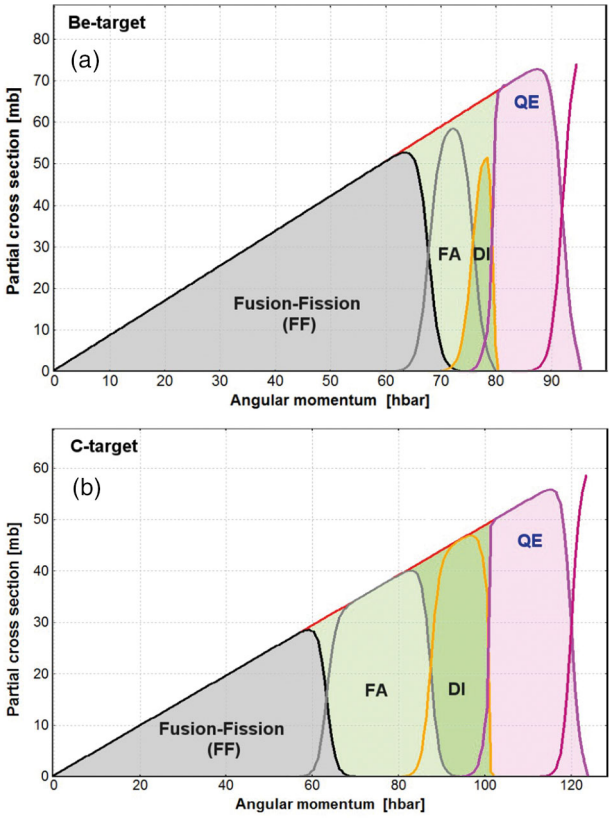

Fig. 10. Partial cross sections calculated by the LISE^{++} code for the reaction of a ^{238}U primary beam at energy 20 MeV/u with beryllium (a) and carbon (b). Channel designation and angular momentum values are given in table 1. Cross section values are summarized in table 4.

In general, the main trends of the experimental data (see fig. 9) are fairly well reproduced by the LISE^{++} calculations. The calculations show that (76%) fusion-fission should dominate fast-fission in the case of Be-target, whereas the picture changes rapidly if the target becomes a little bit heavier as in the carbon target case: domination of fast-fission (59%) over complete fusion-fission due to the drastic increase of the fast-fission contribution (see fig. 10). This analysis indicates that the difference in elemental experimental distributions of fragments produced with two different light targets could be explained by larger a fast-fission component with the carbon target due to the formation of a significant number of nuclei with a vanishing fission barrier.

4.4 Compound nucleus formation and yield as a function of a primary beam energy

The present work shows that different reaction mechanisms are important for the same projectile velocity with two light targets that are relatively close in mass number. Reaction parameters that are not energy dependent such as the Bass interaction radii [21] (Be: 11.9 and C: 12.1 fm) and the angular momenta where the fission barriers vanish (Be: 67 $\hbar$ and C: 63 $\hbar$, see table 1) are very similar. Comparison of the partial cross section distributions in fig. 10 indicates that the difference comes from the energy dependence of the maximum angular momenta and the slope of the partial cross sections function. The same effect was seen before in "direct" kinematics with light projectiles and heavy target [33] but is a much stronger effect when observed in inverse kinematics as in this work. For example, the moment of inertia of two nuclei at the interaction distance R_{int} in the case of light targets $A_p \gg A_t$ can be written as

$$I = \mu R_{int}^2 \cong m_t R_{int}^2, \tag{3}$$

where is $\mu = m_t m_p/(m_t + m_p)$ is the reduced mass of the projectile and target system and is very nearly equal to the mass of the target in the present cases. The maximum angular momentum using the approximate moment of inertia from eq. (3) is

$$L_{max} \cong m_t R_{int} \upsilon, \tag{4}$$

where υ is the projectile velocity in the laboratory system. The ratio of maximum angular momenta of two light targets at the same projectile velocity with the additional assumption that $R_{int\_1} \cong R_{int\_2}$ is then proportional to the target masses. Designating $E_{B_f=0}$ as the beam energy corresponding to $L_{max} = L_{B_f=0}$ and assuming that the capture cross section, $\sigma_{capture}$, does not change at energies above $E_{B_f=0}$, the CN formation cross section can be written as

$$\sigma_{CN} = \left(\frac{L_{B_f=0}}{L_{max}}\right)^2 \sigma_{capture}. \tag{5}$$

The ratio of CN formation cross sections in the case of two light targets with a single heavy primary beam at energies above $E_{B_f=0}$ is proportional to the square of their mass ratio (see fig. 11) neglecting small differences between $L_{B_f=0}$, and $\sigma_{capture}$ for the two cases

$$\frac{\sigma_{CN\_1}}{\sigma_{CN\_2}} \sim \left(\frac{m_{t\_1}}{m_{t\_2}}\right)^2. \tag{6}$$

This ratio is not a function of projectile energy as can be seen in fig. 11, where the LISE^{++} calculated CN formation cross sections for the reaction of ^{238}U projectiles with light targets are shown as a function of primary beam energy. In the present case of carbon and beryllium targets this ratio is equal to 1.8.

Given this simple geometrical picture of the limitation to CN formation, one can try to identify the best bombarding energy for a given target to produce the CN. Note also that the high atomic number of the beam leads to a relatively large energy loss in the target. The number of target atoms, n_0, in the thickness that corresponds to a 1 MeV/u loss of primary beam energy can be calculated using the inverse stopping power function $(\mathrm{d}E/\mathrm{d}x)^{-1}$ (mg/cm^2)/MeV as

$$n_0 = \frac{N_A}{A_t}\left(\frac{\mathrm{d}E}{\mathrm{d}x}\right)^{-1} \mathrm{MeV}^{-1}, \tag{7}$$

where N_A is Avogadro's constant, and A_t is the target mass number. One can then calculate the CN yield with

Table 4. Partial cross sections (in mb) calculated by the LISE^{++} code for the reaction of a ^{238}U beam at energy 20 MeV/u with beryllium and carbon targets (see fig. 10). The Sierk model [24] has been used to estimate a fission barrier dependence from angular momentum.

Reaction channel	Be target	C target
Complete fusion-fission (FF)	1987	1016
Fast-fission (FA+DI)	643 (494 + 149)	1455 (913 + 542)
Quasi-elastic (QE)	878	1013
Ratio FF/(FF+FA)	75.5%	41.1%

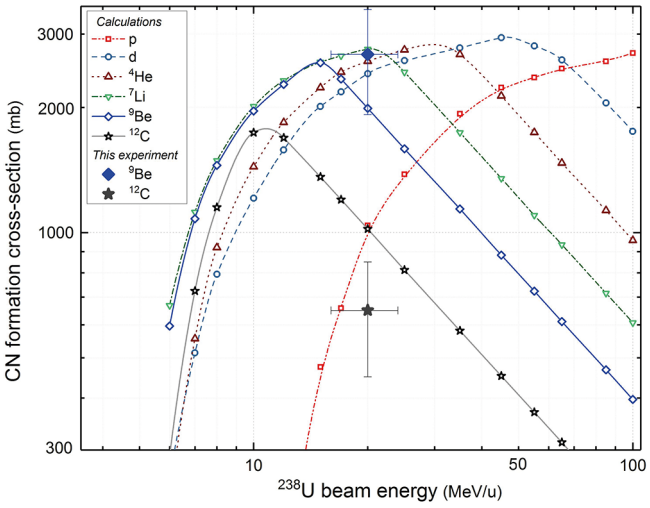

Fig. 11. LISE^{++} calculated CN formation cross sections for the reaction of ^{238}U projectiles with various light targets as a function of a primary beam energy (curves) and the results with Be and C targets obtained in the current experiment (points with uncertainties).

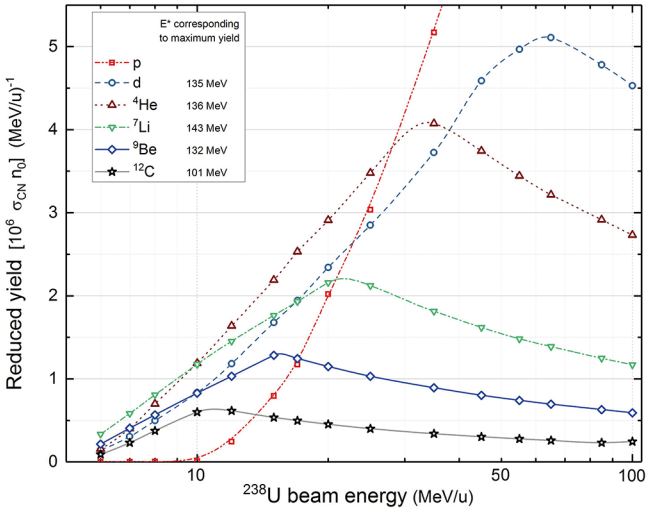

Fig. 12. Calculated CN formation rates in reaction of ^{238}U projectiles with various light targets as function of a primary beam energy. See text for details.

a beam particle fluence, Φ, as

$$Y(E) = \Phi n_0(E)\sigma_{CN}(E)\,\mathrm{MeV}^{-1}. \quad (8)$$

The calculated CN formation rates from the reaction of ^{238}U projectiles with a variety of light targets are shown as a function of a primary beam energy in fig. 12 for a beam fluence of 10^6. The excitation energy values corresponding to maximum yields are given in the figure legend. Each yield curve has a maximum value that depends on the angular momentum value where the fission barrier goes to zero.

The fusion-fission elemental distribution also becomes broader with increasing primary beam energy since the CN excitation energy increases and the products become less neutron-rich (see fig. 13). Therefore, the production of high-Z, neutron-rich nuclei depends more on the excitation energy factor that the overall CN formation cross sections and target thickness.

For example, fig. 13 shows that the production more neutron-rich isotopes in fusion-fission reactions with ^{238}U beam and a Be-target is highest at an energy of ~ 15 MeV/u, which is close to the energy corresponding to the maximum yield with a beryllium target. The excitation energies corresponding to the maximum yields are

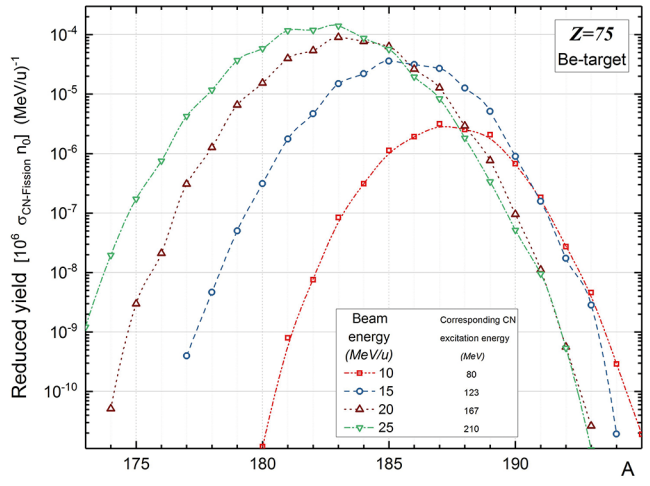

Fig. 13. Reduced yield of rhenium ($Z = 75$) isotopes calculated by the LISE^{++} code for fusion-fission fragments produced in reaction of the ^{238}U ions at energies 10, 15, 20, 25 MeV/u with a Be target.

indicated in the legend of fig. 12 and are generally similar for these targets which suggests similar distribution shapes (position and width) for rhenium isotopes would be observed at energies corresponding to the maximum yields in fig. 12.

5 Summary

Fusion-Fission reaction products produced by a ^{238}U beam at 24 MeV/u on ^{9}Be and $^{\text{natural}}$C targets were measured in inverse kinematics with the LISE3 fragment separator. Identification of fragments was done using the *ΔE-TKE-Bρ-ToF* method. Germanium gamma-ray detectors were placed in the focal plane near the Si stopping telescope to provide an independent verification of the isotope identification via isomer tagging. The experiment demonstrated excellent resolution in Z, A, and q. The results demonstrate that a fragment separator can be used to produce radioactive beams using fusion-fission reactions in inverse kinematics, and further that in-flight fusion-fission can become a useful production method to identify new neutron-rich isotopes, investigate their properties and study production mechanisms. Mass and atomic number distributions are given for both reactions.

The comparison of the experimental atomic and neutron number distributions combined with a partial-wave cross section analysis indicates that the reaction mechanism changes substantially between the ^{9}Be and $^{\text{natural}}$C targets, evolving from complete fusion-fission to fast-fission.

The current analysis using two exit channels and a combined transmission shows only fair agreement between experimental data and calculations by LISE^{++}. The analysis was expanded to include a large contribution from fast-fission that occurs when the fission barrier vanishes due to increasing angular momentum in the case of the carbon target.

The data suggest that complete fusion-fission is mostly responsible for the production of fragments with $Z > 60$ in the case of Be and C targets at 20 MeV/u and this reaction may be used to produce neutron-rich rare-isotope beams in future studies. Geometrical calculations of the CN formation cross-section with light targets as a function of ^{238}U projectile energy show that the target material determines the yields of neutron-rich high-Z isotopes through the excitation energy distribution.

The authors would like to acknowledge Dr. G.N. Knyazheva (FLNR/Dubna) for fruitful discussions. This work was supported by the US National Science Foundation under Grants No. PHY-06-06007, No. PHY-10-68217, No. PHY-11-02511, and No. PHY-15-65546.

References

1. M. Bernas *et al.*, Phys. Lett. B **415**, 111 (1997).
2. M. Hesse *et al.*, Z. Phys. A **355**, 69 (1996).
3. O.B. Tarasov, D. Bazin, Nucl. Instrum. Methods Phys. Res. B **266**, 4657 (2008) http://lise.nscl.msu.edu/.
4. M. Caamaño *et al.*, Phys. Rev. C **88**, 024605 (2013).
5. A. Shrivastava *et al.*, Phys. Rev. C **80**, 051305(R) (2009).
6. F. Farget *et al.*, Eur. Phys. J. A **51**, 175 (2015).
7. C. Rodriguez-Tajes *et al.*, Phys. Rev. C **89**, 024614 (2014).
8. O.B. Tarasov, A.C.C. Villari, Nucl. Instrum. Methods Phys. Res. B **266**, 4670 (2008).
9. R. Anne *et al.*, Nucl. Instrum. Methods A **257**, 215 (1987).
10. M.G. Itkis *et al.*, Nucl. Phys. A **944**, 201 (2015).
11. M.G. Itkis *et al.*, Int. J. Mod. Phys. E **16**, 957 (2007).
12. R.G. Thomas *et al.*, Phys. Rev. C **77**, 034610 (2008).
13. J. Khuyaagbaatar *et al.*, Phys. Rev. C **91**, 054608 (2015).
14. V.I. Zagrebaev, W. Greiner, Phys. Rev. C **78**, 034610 (2008).
15. V.I. Zagrebaev, Nucl. Phys. A **734**, 164 (2004).
16. J.P. Block *et al.*, Nucl. Phys. A **459**, 145 (1986).
17. W.J. Swiatecki, Phys. Scr. **24**, 113 (1981).
18. S. Bjornholm, W. Swiatecki, Nucl. Phys. A **391**, 471 (1982).
19. O.B. Tarasov *et al.*, Phys. Rev. C **80**, 034609 (2009).
20. O.H. Odland *et al.*, Nucl. Instrum. Methods Phys. Res. A **378**, 149 (1996).
21. R. Bass, Nucl. Phys. A **231**, 45 (1974).
22. J.R. Birkelund *et al.*, Phys. Rev. C **13**, 133 (1976).
23. O.B. Tarasov, private communication, *Update of fusion reaction mechanism in LISE*$^{++}$, available on-line at `http://lise.nscl.msu.edu/9_10/9_10_Fusion.pdf`.
24. A.J. Sierk, Phys. Rev. C **33**, 2039 (1986).
25. D.J. Morrissey *et al.*, Nucl. Phys. A **442**, 578 (1985).
26. A. Leon *et al.*, At. Data Nucl. Data Tables **69**, 217 (1998).
27. G. Schiwietz, P.L. Grande, Nucl. Instrum. Methods Phys. Res. B **175**, 125 (2001).
28. J.A. Winger, B. Sherrill, D.J. Morrissey, Nucl. Instrum. Methods Phys. Res. B **70**, 380 (1992).
29. O.B. Tarasov, *Abrasion-Fission*, NSCL preprint MSUCL1316 (2005) `https://groups.nscl.msu.edu/nscl_library/nscl_preprint/MSUCL1300.pdf`.
30. J. Pereira *et al.*, Phys. Rev. C **75**, 044604 (2007).
31. M. Bernas *et al.*, Nucl. Phys. A **725**, 213 (2003).
32. K.-H. Schmidt, J. Benlliure, A.R. Junghans, Nucl. Phys. A **693**, 169 (2001).
33. M. Lefort, Nucl. Phys. A **387**, 3 (1982).